The Bioscan AN INTERNATIONAL QUARTERLY JOURNAL OF LIFE SCIENCES 20(4): 2351-2377, 2025 www.thebioscan.com

Microscopic-Macroscopic Modelling of Dispersion and Optical Anisotropy in $LiNbO_3$ and $LiIO_3$ Using the Point Dipole Approximation

Chilukuri Nagender [a, b], ***A.Raju*** [a], ***D. Suresh*** [a*], ***Ravindharan Ethiraj*** [c]
[a]*Department of Physics & Electronics, Chaitanya (Deemed to be University), Himayathnagar (V), Moinabad (M), Ranga Reddy (D), Telangana, India*
[b]*Department of Freshman Engineering , KPRIT College of Engineering, Hyderabad, Telangana, India*
[c]*Department of Physics, Nizam College, Hyderabad, Telangana, India*
*Corresponding Author Email: ***suresh.domala@gmail.com***

DOI: https://doi.org/10.63001/tbs.2025.v20.i04.pp2351-2377

KEYWORDS
Uniaxial ferroelectric crystals ($LiNbO_3$ and $LiIO_3$), refractive index dispersion, point-dipole approach model, electronic polarizability, waveguide optical anisotropy

Received on:
30-11-2025
Accepted on:
18-12-2025
Published on:
28-12-2025

Abstract
This study aims to establish a unified understanding of the wavelength-dependent optical properties of the uniaxial ferroelectric crystals $LiNbO_3$ and $LiIO_3$, with the objective of improving material selection and optimization for electro-optic and nonlinear photonic applications. By integrating the Point Dipole Approximation (PDA) with Sellmeier dispersion formulations, the ordinary refractive index (n_o), extraordinary refractive index (n_e) birefringence ($\Delta n = n_e - n_o$), and the corresponding polarizabilities were systematically determined over the wavelength range of 436-3391 nm. The results show a monotonic decrease in n_o and n_e with wavelength for both materials, while $LiNbO_3$ consistently exhibits higher refractive indices and birefringence than $LiIO_3$ due to the smaller and more strongly polarizing Nb^{5+} ion. At λ = 633 nm, the PDA-reconstructed indices show excellent agreement with experimental data (e.g., $LiNbO_3$: $n_o = 2.2846$, $n_e = 2.2124$; $LiIO_3$: $n_o = 2.2459$, $n_e = 2.2102$), validating the model. These findings highlight that crystal structure and ionic radius fundamentally govern optical anisotropy, confirming $LiNbO_3$ as more suitable for electro-optic modulation, whereas $LiIO_3$ is better suited for high-power nonlinear optical applications. Overall, this work provides a predictive, structure-based tool for designing and engineering advanced photonic and optoelectronic devices.

1. Introduction
Ferroelectric optical materials are integral to contemporary photonic and optoelectronic technologies, underpinning numerous advanced applications ranging from optical communication systems to ultrafast photonic devices.[1] Lithium Niobate ($LiNbO_3$) and lithium iodate ($LiIO_3$) are widely recognized as key uniaxial ferroelectric crystals in optical engineering. A detailed understanding of their wavelength-dependent optical characteristics is therefore essential for the effective optimization of device performance across diverse spectral regimes.[2] Owing to their non-centrosymmetric crystal structures, these materials display pronounced Pockels electro-optic responses, significant piezoelectric behaviour, and strong nonlinear optical coefficients, rendering them indispensable for both classical and quantum photonic applications.[3] The refractive indices and birefringence characteristics of these crystals directly determine their suitability for specific optical applications, requiring comprehensive characterization across broad spectral ranges to enable optimal material selection and device design.[4] The rapid advancement of integrated photonics and optoelectronic devices has created an increasingly pressing need for detailed, wavelength-dependent optical characterization of ferroelectric materials.[5]

$LiNbO_3$ is distinguished by its strong electro-mechanical response, including prominent Pockels and photoelastic effects, which underpin its widespread use in electro-optic modulators, Q-switches, and wavelength-conversion devices.[6] These applications demand precise knowledge of refractive indices across wide spectral ranges to enable accurate device modelling and engineering. Similarly, $LiIO_3$ exhibits unique advantages for high-power nonlinear optical applications due to its favourable phase-matching properties and high optical damage threshold, yet comprehensive dispersion data across visible to infrared wavelengths remains limited. The broad optical transparency of both materials, extending from ultraviolet (0.35 μm) to mid-infrared (5.3 μm) for $LiNbO_3$ and 0.5 to 5.0 μm for $LiIO_3$, necessitates systematic investigation of how optical properties vary across this extensive spectral range.[7] Such comprehensive characterization is essential for the efficient design of integrated optical circuits, waveguides, and optical parametric devices operating across multiple wavelength regions.[8]

Considerable research has been devoted to characterizing the optical properties of $LiNbO_3$ and $LiIO_3$ crystals, with many studies focusing on specific spectral regions or particular applications. $LiNbO_3$ has been widely studied for electro-optic modulation, particularly in waveguide modulators and resonator-based devices used in telecommunications and operated with Nd:YAG, Nd:YLF, and Ti:sapphire laser systems.[9] Its large nonlinear optical coefficients have established the material as a standard platform for frequency-conversion processes, including second- and higher-harmonic generation from the visible to ultraviolet regions, as well as optical parametric oscillators producing tunable mid-infrared radiation under 1064 nm pumping.[10] In ultrafast optics, $LiNbO_3$ serves as a medium for autocorrelators and pulse diagnostic systems for femtosecond Ti:Sapphire and Nd:YAG lasers, where precise phase and amplitude control are essential.[11] Moreover, the stability and high electro-optic efficiency of $LiNbO_3$ make it a preferred substrate for planar waveguides and surface acoustic wave (SAW) devices, supporting the development of compact integrated photonic circuits.[12] Regarding $LiIO_3$, while earlier research demonstrated its remarkable potential for frequency-doubling applications and nonlinear optics, fewer systematic studies have provided comprehensive wavelength-dependent characterization compared to the extensive $LiNbO_3$ literature.[13] Existing literature typically presents refractive index values at discrete wavelengths (such as measured values at 1064 nm: n_o =2.232, n_e =2.156 for congruent $LiNbO_3$, and n_o =1.8571, ne=1.7165 for $LiIO_3$), rather than detailed dispersion relationships across broad spectral ranges.[14] While previous experimental measurements have provided refractive index data at specific isolated wavelengths, a critical research gap exists regarding comprehensive, continuous characterization of wavelength-dependent optical properties across the full visible to infrared spectrum for both materials simultaneously.[15] Most prior studies have either concentrated on $LiNbO_3$ with limited attention to $LiIO_3$, or have presented data only at discrete wavelengths rather than systematic dispersion relationships.[16]

Furthermore, the comparative analysis of how material differences, particularly the larger ionic radius of iodine compared to niobium, systematically influence optical properties across wavelengths has not been thoroughly explored in a unified theoretical framework.[17] Traditional experimental approaches face inherent limitations in providing data across extremely broad spectral ranges.[18] And there is a pressing

need for theoretical models that can bridge experimental measurements across different spectral regions and enable interpolation and extrapolation of optical properties. Additionally, while the local field effects at crystal surfaces and in waveguides differ from bulk properties, previous studies have not adequately addressed how these surface-to-bulk variations influence refractive indices and polarizabilities in optical waveguides, a critical consideration for thin-film and integrated optical device applications.[19] The relationship between ionic properties (particularly ionic radius and polarizability) and macroscopic optical response also remains incompletely characterized, limiting the ability to design new ferroelectric materials with optimized optical properties.[20]

To address these research gaps, this work employs the point dipole approximation (PDA) combined with Sellemier dispersion relations as a sophisticated theoretical framework for comprehensive optical characterization. The PDA approach is particularly well-suited for ferroelectric materials because it directly relates macroscopic optical properties to the microscopic polarizabilities of constituent ions, providing fundamental insights into structure-property relationships.[21] By systematically varying ionic polarizabilities and calculating lattice anisotropy factors through geometric summations of dipole-dipole interactions, the PDA enables precise determination of refractive indices across extremely broad wavelength ranges[22,23]. This approach has the advantage of accounting for local field effects that differ between surface and bulk environments, which is particularly important for understanding optical waveguide behaviour where the effective optical properties depend on the spatial distribution of ions.[24, 25]

A comparative analysis of $LiNbO_3$and $LiIO_3$ within a unified theoretical framework provides new insight into how ionic variations, specifically the size contrast between Nb^{5+} (0.764 Å) and I^{5+} (0.928 Å), manifest in macroscopic optical anisotropy and polarisability-driven optical response. This material comparison is uniquely valuable because both crystals share the same basic ferroelectric functionality and crystal symmetry characteristics, yet exhibit notably different optical properties due to their compositional differences, providing an excellent natural experiment for understanding fundamental structure-property relationships in uniaxial ferroelectrics[26].

The main aim of this work is to perform a systematic wavelength-dependent investigation of the optical properties namely the ordinary refractive index (n_o), extraordinary refractive index (n_e), birefringence (Δn), and ionic polarizabilities of $LiNbO_3$ and $LiIO_3$ over the spectral range 436 –3391 nm using the point dipole approximation in conjunction with Sellmeier dispersion relations. More specifically, it aims to:

- Systematically compute refractive indices and birefringence for both materials across the visible, near-infrared, and infrared spectral regions.
- Determine the wavelength-dependent ionic polarizabilities of Li^+, Nb^{5+}/I^{5+}, and O^{2-} ions through iterative application of the PDA.
- Provide quantitative comparison of how the larger ionic radius in $LiIO_3$ influences optical anisotropy relative to $LiNbO_3$
- Develop predictive models that can accurately describe optical properties across wavelengths where experimental data may be scarce or difficult to obtain.

This work establishes a continuous microscopic–macroscopic optical dispersion model for Li-based uniaxial ferroelectric waveguides, addressing the long-standing scarcity of unified, continuous refractive-index (n_o, n_e) and birefringence (Δn) characterization across broadband wavelengths. Using a self-consistent point-dipole local-field framework constrained by Lorentz-Lorenz equation, the study quantifies how lattice spacing and central-ion radius govern polarisability-driven optical response and optical anisotropy, providing a physically interpretable origin for spectral dispersion.[27, 28] The results confirm the higher index, polarizing field strength, and birefringence of $LiNbO_3$ relative to the lower-index, weaker-anisotropy behaviour of $LiIO_3$. While limited by a spherical cavity assumption and exclusion of far-IR vibrational terms, the method reproduces visible-band benchmarks with high fidelity. Key outcomes are the confirmed wavelength decay of polarisability-driven optical response and central-ion-driven anisotropy contrast, enabling predictive, structure-encoded material assessment for integrated nonlinear and electro-optic photonics.

2. Methods

2.1 Implementation of Periodic Boundary Conditions

The Point Dipole Approximation (PDA) requires evaluation of the local electric field at a reference ionic site as a sum of contributions from all surrounding dipoles in the crystal lattice. Because a real crystal is effectively infinite, these lattice summations must, in principle, extend to infinity. Periodic boundary conditions (PBC) are implemented here using a supercell replication approach: the unit cell, defined by the fractional atomic coordinates given in Table 2, is replicated in all three spatial dimensions. The dipole-field contributions from periodic images are accumulated systematically over an expanding sphere of radius r (the cavity radius), as detailed in the convergence study of Table 3 and Figure 2.

Computationally, the C++ code implements PBC as follows. (i) Fractional atomic coordinates for each ionic species (Li^+, Nb^{5+}/I^{5+}, O^{2-}) are read from separate input files (li.dat, nb.dat, o.dat). (ii) Supercell images are generated by iterating over integer translation vectors (e, f, g) from $-q_{max}$ to $+ q_{max}$ (q_{max} = 12 lattice spacings) in three nested loops. (iii) Fractional coordinates are converted to Cartesian coordinates using the hexagonal lattice parameters a = 7.119 Å and c = 6.29 Å. (iv) The dipole-field tensor components $(3x^2 - r^2)/r^5$ are accumulated for all ions within the real-space cutoff $r_{cut} = n_{max}$ a (n_{max} = 10). (v) Self-interactions (u = v = w = 0 when source and target atoms are identical) are excluded. The resulting sums yield the lattice anisotropy factors D_{ij} presented in Table 4.

This approach assumes a spherical cavity approximation, which is well justified for the near-isotropic short-range ionic environment of both $LiNbO_3$ and $LiIO_3$[29]. A limitation is that no Ewald summation correction for the long-range dipolar tail is applied; however, the convergence study (Table 3) confirms that the real-space cutoff at approximately 70 Å accounts for all significant contributions, with further extensions changing D_{ij} by less than 1% (see Table 3 and Figure 2).

2.2 Sellmeier Dispersion Parameters

The Sellmeier dispersion equation used in this work has the general two-oscillator form, comprising one UV electronic term and one long-wavelength IR approximation term:

$$n^2(\lambda) = A + B_1 / (C_1 - \lambda^2) - B_2\lambda^2 \quad (1)$$

where λ is the vacuum wavelength in micrometres[30]; A is the high-frequency background dielectric constant that accounts for the contributions of all absorption resonances lying well outside the measured spectral range; B_1 is the dimensionless UV oscillator strength associated with electronic transitions near the band edge; C_1 is the square of the UV resonance wavelength (μm²), so that $\sqrt{C_1}$ gives the effective UV absorption edge wavelength; and B_2 is the IR dispersion coefficient arising from phonon-polariton resonances at wavelengths well beyond the transparency window. The negative IR term $-B_2\lambda^2$ is the long-wavelength ($\lambda \ll \lambda_{IR}$) approximation of the full Sellmeier IR oscillator term $-B_2\lambda^2/(\lambda^2 - C_2)$, valid when $\lambda \ll \sqrt{C_2}$. For both $LiNbO_3$ and $LiIO_3$, the IR resonance wavelengths $\sqrt{C_2}$ lie in the range 4.8–6.7 μm (Table 1), well beyond the upper limit of the present study (3.391 μm), confirming that this approximation introduces negligible error across the entire modelled spectral range. The IR resonance wavelength C_2 listed in Table 1 is therefore a physically derived quantity, recovered from the fitted B_2 coefficient via the limiting relationship $C_2 \approx B_2/B_2$, full rather than an independently fitted parameter appearing in Equation (1). The sign convention adopted here (positive UV term with denominator $(C_1 - \lambda^2)$ and negative IR term $-B_2\lambda^2$) follows directly from the parameterisations reported in the source references.[22, 23]

Table 1 presents the Sellmeier coefficients for all four polarisation modes (A, B_1, C_1, B_2), together with the UV and IR resonance wavelengths ($\sqrt{C_1}$ and $\sqrt{C_2}$) derived from the fitted parameters. The IR resonance wavelength $\sqrt{C_2}$ is a physically interpreted quantity recovered from the B_2 coefficient, as described above; it does not appear as an independent fitted term in Equation (1).

Table 1. Sellmeier coefficients for $LiNbO_3$ and $LiIO_3$

Crystal & Polarisation	A	B_1 (UV oscillator)	$\sqrt{C_1}$ (μm) UV resonance	B_2 (IR oscillator)	$\sqrt{C_2}$ (μm) IR resonance	Source
$LiNbO_3$ (ordinary)	4.9048	0.11768	0.218	0.02717	6.07	[22]
$LiNbO_3$ (extraordinary)	4.5820	0.09917	0.211	0.02195	6.74	[22]
$LiIO_3$ (ordinary)	3.1531	0.05124	0.188	0.02691	6.09	[23]
$LiIO_3$ (extraordinary)	3.0012	0.03450	0.180	0.04314	4.82	[23]

IR resonance wavelength = $\sqrt{C_2}$ in μm; values > 4 μm are consistent with phonon-polariton absorption beyond the transparency window

2.3 Justification of the Spectral Range

The spectral range of 436–3391 nm for $LiNbO_3$ and 476–3247 nm for $LiIO_3$ was selected on the basis of three complementary considerations: the transparency windows of the materials, the validated range of the adopted Sellmeier equations, and the availability of standard laser wavelengths for benchmarking. $LiNbO_3$ is transparent from approximately 0.30 μm (UV absorption edge) to 5.3 μm (multi-phonon absorption edge), and $LiIO_3$ from approximately 0.37 μm to 5.0 μm.[6, 30] While both crystals are transparent at wavelengths shorter than 436 nm, the Sellmeier equations

adopted in this work were validated against experimental data in the 436–3391 nm range.[22, 23] Extending the model below 400 nm would require alternative temperature-dependent Sellmeier parameterisations validated near the UV absorption edge, such as those reported for $LiNbO_3$[28, 31]; this is left for future work. The selected spectral range is directly relevant to the principal nonlinear optical applications of both crystals. Both $LiNbO_3$ and $LiIO_3$ are widely used as media for second-harmonic generation (SHG) of Nd:YAG (1064 nm) and Ar-ion (514 nm) laser sources, producing outputs in the visible and near-UV ranges that fall within the modelled window[27]. $LiNbO_3$ is also routinely employed in the quasi-phase-matching configuration (periodically poled $LiNbO_3$, PPLN) to generate narrowband UV radiation at wavelengths as short as 400 nm[32]. $LiIO_3$ is particularly attractive for broadband SHG of ultrashort laser pulses into the near-UV region owing to its wider phase-matching acceptance bandwidth.[30]. The present PDA model, constrained to the 436–3391 nm window, therefore captures the spectral regime most relevant to these applications and establishes the framework that can be extended towards the UV when the appropriate Sellmeier parameterisations become available.

2.4 Point Dipole Approximation: Theory

The point dipole approximation (PDA) is employed to link the crystal refractive indices, derived from Sellmeier relations, to the polarizabilities of the constituent ions.[29] A key consideration is that the local electric field acting on an ion near the crystal surface differs from that in the bulk crystal environment.[24, 33] As reported in earlier studies, surface ions experience a modified local environment, leading to small variations in refractive index and polarizability between the crystal surface and its bulk. By modelling this variation (for example, by effectively sampling ions from the surface inward), we can more accurately predict the optical behaviour of thin films and waveguides. Our goal is thus to determine n_o, n_e, Δn and the ion polarizabilities for $LiNbO_3$vs. $LiIO_3$ across the visible–infrared spectrum, and to identify how the larger I^{5+} ion in $LiIO_3$ influences these properties. These findings offer valuable guidance for the design of advanced optical waveguides and integrated photonic devices based on ferroelectric crystals.[34]

Uniaxial materials constitute a class of anisotropic crystals belonging to the tetragonal and hexagonal crystal systems and are characterized by the presence of a single optic axis.[35] When light propagates along this optic axis, the crystal exhibits isotropic behaviour, in the sense that the polarization state of the light remains unchanged during transmission.[36] As with all anisotropic media, uniaxial crystals possess refractive indices that vary between two limiting values. These are identified as the ordinary refractive index (n_o) and the extraordinary refractive index (n_o). The absolute birefringence of a uniaxial crystal is defined as the magnitude of the difference between these two refractive indices, (n_e - n_o).[37]

Consider $LiNbO_3$ and $LiIO_3$ crystals subjected to an external electric field E_0. Under the influence of the incident electromagnetic radiation, each constituent atom of the crystal acquires an induced dipole moment. These induced moments are associated with individual lattice sites and are modelled as point dipoles within the framework of the Point Dipole Approximation (PDA).[38] Using this approach, the Lorentz local fields at various lattice positions within the unit cell are evaluated by accounting for the

contributions from surrounding atomic dipoles, following methodologies widely adopted in earlier studies.[20]

In this treatment, the Li^+, Nb^{5+}, I^{5+}, and O^{2-} ions are considered as point dipoles. The wavelength-dependent polarizabilities of the Nb^{5+}, I^{5+}, and O^{2-} ions are calculated using the PDA, whereas the polarizability of the Li^+ ion is assumed to be constant. This assumption is justified by its positive ionic nature and comparatively small electronic polarizability relative to the other constituent ions.

The macroscopic electric field is defined as an average over spatial dimensions on the order of 10^{-3}cm, typically encompassing approximately 10^{10} molecules. The magnitude of this macroscopic field depends on both the externally applied field and the geometrical shape of the dielectric medium. In contrast, the local electric field E_{loc} experienced by an individual ion arises from the combined contributions of external sources and the fields generated by all other ions in the crystal, excluding the ion's self-field.[39]

The electric field at the origin due to a collection of dipoles with moments μ_i, located at position vectors r_i, is expressed using the standard dipole field formulation.[40]

$$E_{dipoles} = \sum_i \frac{3(\mu_i r_i) r_i - r_i^2 \mu_i}{r_i^5} \quad (2)$$

which can be resolved into rectangular orthogonal coordinate system

$$E_{x\,dip} = \sum_{ix} \frac{\mu_{ix}(2x_i^2 - y_i^2 - z_i^2)}{r_i^5} = \mu_{ix} \sum_{ix} \frac{3x_i^2 - r_i^2}{r_i^5} \quad (3)$$

$$E_{y\,dip} = \sum_{iy} \frac{\mu_{iy}(2y_i^2 - z_i^2 - x_i^2)}{r_i^5} = \mu_{iy} \sum_{iy} \frac{3y_i^2 - r_i^2}{r_i^5} \quad (4)$$

$$E_{z\,dip} = \sum_{iz} \frac{\mu_{iz}(2z_i^2 - x_i^2 - y_i^2)}{r_i^5} = \mu_{iz} \sum_{iz} \frac{3z_i^2 - r_i^2}{r_i^5} \quad (5)$$

Here, μ_{ix}, μ_{iy} and μ_{iz} denote the components of the dipole moment of the i^{th} ion along the coordinate axes. The local electric field is conveniently expressed as the superposition of the externally applied field and the field produced by dipoles within the crystal. However, it is convenient to write the Local Electric Field as the sum of the electric field from external sources and of the field from the dipoles within the specimen and is given by,

$$E_{loc} = E + E_1 + E_2 + E_3 \quad (6)$$

Here the terms are:

E = External field.

E_1 = The depolarization field arises from induced surface charges on the outer boundary of the specimen.

E_2 = The Lorentz cavity field is the electric field produced by polarization charges on the inner surface of an imaginary spherical cavity cantered on the reference atom within the specimen.

E_3 = This field arises from all dipoles located within the spherical cavity.

The decomposition of the local electric field into its constituent components follows the classical treatment of electromagnetic propagation in dielectric media.[21, 41] The depolarisation field E_1 arises from surface charges induced at the outer boundary of the

specimen. The Lorentz cavity field E_2 is produced by polarisation charges on the inner surface of the imaginary spherical cavity. The field E_3 represents the combined contribution of all individual dipoles within the cavity. The choice of a spherical cavity is justified by the near-isotropic short-range environment, and results in the Lorentz cavity contribution $E_2 = P/3\varepsilon_0$ (Equation 8 below).[21] This formalism links the Lorentz–Lorenz equation to the fundamental electromagnetic theory of polarisable dielectrics, providing the rigorous physical basis for the PDA as applied in this work.

The dimensions of the cavity chosen should be such that they are large compared to the interatomic distance but small compared to the dimensions of the specimen.

We can write $E_{loc} = E + E_2 + E_3$

(7)

Here, E denotes the average macroscopic electric field. Therefore, it may be expressed as

$E = E_0 + E_1$.

For crystals where atoms have cubic symmetry like *Na+* or *Cl-* ions in the *NaCl* type lattice structures, due to spherical symmetry the dipole field summations are $\sum \frac{z_i^2}{r_i^5} = \sum \frac{y_i^2}{r_i^5} = \sum \frac{x_i^2}{r_i^5}$ and The right-hand side of Equation (4) vanishes. As a result, the factor representing the total dipole field from all dipoles inside the cavity becomes zero.

Hence $E_{loc} = E + E_2$

For a spherical cavity, Lorentz demonstrated that $E_2 = P/3\varepsilon_0$.[42]

(8)

where *P* is the Polarization vector.

2.5. Expressions for Refractive Indices: A Point Dipole Approach

The atomic polarizability α is defined through the local electric field at the position of the atom, as given by the relation

$\mu = \alpha E_{loc}$

(9)

Here 'μ' is the dipole moment of the atom. The total polarizability α is expressed as the sum of four terms corresponding to the principal contributions to polarization. Thus,

$\alpha_{tot} = \alpha_e + \alpha_i + \alpha_d + \alpha_s$

Here, α_e denotes electronic polarizability, α_i ionic polarizability, α_d dipolar polarizability, and α_s space-charge polarizability. Electronic polarizability α_e arises from the displacement of the atomic electron cloud relative to the nucleus. Ionic polarizability α_i results from the relative displacement of positive and negative ions under an applied electric field. In the case of molecules having permanent dipole moments (like the hydrogen bonded atoms) the molecules exhibit dipolar polarizability α_d, space charge polarizability α_s , arises from the migration of charge carriers in the dielectric. Dipolar contribution drops out in the microwave region. Since ions are more massive compared to the electrons, the ionic contribution to the polarizability is limited to the region beyond the infrared.[43] Among the four contributions, electronic polarizability is the most dominant and remains significant in the visible and ultraviolet regions. Therefore, only electronic polarization is considered in the present analysis.

To quantify this further: the total electronic polarizability per formula unit at λ = 633 nm for $LiNbO_3$ is $\alpha_{tot} = \alpha Li^+ + \alpha Nb^{5+} + 3\alpha O^{2-} = 0.0290 + 1.2666 + 3 \times 2.0044 = 7.3088 \times 10^{-24}$ cm³. Since all polarizability values in the optical frequency range were determined under the assumption of a purely electronic response, the electronic contribution constitutes ≥99.9% of the fitted polarizability budget at optical frequencies. This is physically consistent: ionic (phonon-

driven) polarizability only contributes at frequencies below the phonon resonance (typically $\lambda > 5$ μm), well outside the modelled spectral range[44]. In the optical regime, electronic polarisation therefore dominates the dielectric response overwhelmingly, confirming the validity of considering only electronic polarizability in the present PDA analysis.

Equation (9) may be expressed as $\mu_j = \alpha_j (E+E_2+E_3)_j$, where the bracketed term denotes the local electric field at the site of the j^{th} ion. Accordingly, the polarization P can be written as,

$$P = \sum_j N_j \mu_j = \sum_j N_j \alpha_j (E + E_2 + E_3)_j \quad (10)$$

Here, N_j denotes the number of ions of type j per unit volume. Expanding the above

$$P = \sum_j N_j \alpha_j E + \sum_j N_j \alpha_j E_2 + \sum_j N_j \alpha_j E_{3j} \quad (11)$$

Here, E_{3j} represents the electric field due to all dipoles inside the cavity, with the ion located at its center. This term constitutes the right-hand side of Equation (2). Considering the x-component of the above expression, we obtain,

$$P_x = [\sum_j N_j \alpha_j E + \sum_j N_j \alpha_j E_2 + \sum_j N_j \alpha_j E_{3j}]_x \quad (12)$$

Substituting for E_{2x} from the equation we get,

$$P_x = \left[\sum_j N_j \alpha_j E_x + \left(\sum_j N_j \alpha_j\right) K_x P_x + \sum_j N_j \alpha_j \left(\sum_i \frac{3x_i^2 - r_i^2}{r_i^5} \mu_i\right)\right]_x \quad (13)$$

$$P_x = [\sum_j N_j \alpha_j E_x + (\sum_j N_j \alpha_j) K_x P_x + \sum_j N_j \alpha_j (\sum_i D_{ij} \mu_i)]_x \quad (14)$$

Here $\sum_i D_{ij} = \sum_i \frac{3x_i^2 - r_i^2}{r_i^5}$ It is a measure of the geometric anisotropy in the x-direction for all the i^{th} ions with j^{th} ions at the centre. This quantity may be referred to as the lattice anisotropy factor, while represents the depolarization factor for a spherical cavity.[45] The final term in the above expression can be further expanded as

$$[\sum_j N_j \alpha_j \sum_i D_{ij} \mu_i]_x = [\sum_j N_j \alpha_j \sum_i D_{ij} \alpha_i E_{loc(i)}]_x$$
$$= [\sum_j N_j \alpha_j \sum_i D_{ij} \alpha_i (E + E_2 + E_{3(i)})]_x$$
$$= [\sum_j N_j \alpha_j \sum_i D_{ij} \alpha_i E_x + \sum_j N_j \alpha_j \sum_i D_{ij} \alpha_i K_x P_x + \sum_j N_j \alpha_j \sum_i D_{ij} \alpha_i E_{3(i)}]_x \quad (15)$$

By substituting Equation (14) into Equation (13) and rearranging the terms, we obtain

$$P_x = [\sum_j N_j \alpha_j E_x (1 + \sum_i D_{ij} \alpha_i) + \sum_j N_j \alpha_j K_x P_x (1 + \sum_i D_{ij} \alpha_i) + \sum_j N_j \alpha_j \sum_j D_{ij} \alpha_i E_{3(i)}]_x \quad (16)$$

Here, this term represents the dipole field due to all ions within the cavity, with the reference ion taken as the origin. It can be expanded in a manner identical to that used in Equation (13) *viz* $E_{3(i)} = \sum D_{ik} \alpha_k$. Hence, the final term in Equation (16) may be expressed as $\sum_j N_j \alpha_j \sum_i D_{ij} \alpha_i \sum D_{ik} \alpha_k$. This type of expansion can be continued ad infinitum. It has to be truncated somewhere. Since the magnitudes of these quantities are of the order of 10^{-24}, the final term in the above expression consists of products of three such terms and is therefore comparatively small to the other terms which contain only products of two 's, the last term can be ignored without any loss of accuracy. Therefore, Equation (16) can be rewritten as

$$P_x = [\sum_j N_j \alpha_j E_x (1 + \sum_i D_{ij} \alpha_i) + \sum_j N_j \alpha_j K_x P_x (1 + \sum_i D_{ij} \alpha_i)]_x \quad (17)$$

For an isotropic or cubic medium, the electric susceptibility and the dielectric constant are related by the expression.

$$\chi = \frac{P}{E} = \frac{\varepsilon - 1}{4\pi} \quad (18)$$

In a non-cubic crystal, the dielectric behaviour is characterized by the tensor components of electric susceptibility or dielectric constant. When referred to the crystallographic axes X, the above equation can be written as three equations along the three crystallographic axes as

$$\chi_x = \frac{P_x}{E_x} = \frac{\varepsilon_x - 1}{4\pi}$$

$$\chi_y = \frac{P_y}{E_y} = \frac{\varepsilon_y - 1}{4\pi}$$

$$\chi_z = \frac{P_z}{E_z} = \frac{\varepsilon_z - 1}{4\pi}$$

(19)

Since the present analysis focuses on electronic polarizabilities, *x, y* and *z* can be replaced by n_x^2, n_y^2 and n_z^2 respectively These correspond to the refractive indices for light polarized along the crystallographic axes X, Y, and Z. Equation (16) after rearrangement can be written as

$$\chi_x = \frac{P_x}{E_x} = \frac{n_x^2 - 1}{4\pi} = \frac{\sum_j N_j \alpha_j [1 + \sum_i D_{X ij} \alpha_i]}{1 - \sum_j N_j \alpha_j [1 + \sum_i D_{X ij} \alpha_i] K_x}$$

(20)

OR

$$n_x = \left[\left(\frac{4\pi \sum_j N_j \alpha_j \left[1 + \sum_i D_{X ij} \alpha_i\right]}{1 - \sum_j N_j \alpha_j \left[1 + \sum_i D_{X ij} \alpha_i\right] K_x} \right) + 1 \right]^{1/2}$$

(21)

Similarly, the refractive indices for an electric field polarized along the crystallographic Y and Z axes are given by,

$$\frac{n_y^2 - 1}{4\pi} = \frac{\sum_j N_j \alpha_j [1 + \sum_i D_{Y ij} \alpha_i]}{1 - \sum_j N_j \alpha_j [1 + \sum_i D_{Y ij} \alpha_i] K_y}$$

(22)

OR

$$n_y = \left[\left(\frac{4\pi \sum_j N_j \alpha_j \left[1 + \sum_i D_{Y ij} \alpha_i\right]}{1 - \sum_j N_j \alpha_j \left[1 + \sum_i D_{Y ij} \alpha_i\right] K_y} \right) + 1 \right]^{1/2}$$

(23)

Similarly,

$$\frac{n_z^2 - 1}{4\pi} = \frac{\sum_j N_j \alpha_j [1 + \sum_i D_{Z ij} \alpha_i]}{1 - \sum_j N_j \alpha_j [1 + \sum_i D_{Z ij} \alpha_i] K_z}$$

(24)

OR

$$n_z = \left[\left(\frac{4\pi \sum_j N_j \alpha_j \left[1 + \sum_i D_{Z ij} \alpha_i\right]}{1 - \sum_j N_j \alpha_j \left[1 + \sum_i D_{Z ij} \alpha_i\right] K_z} \right) + 1 \right]^{1/2}$$

(25)

where, $K_x = K_y = K_z = 4\pi/3$ since a spherical cavity is assumed.[46] Using Equations (19), (22), and (25), the refractive indices n_x, n_y, and n_z can be determined by evaluating the lattice anisotropy factors ΣD_{ij} for the different ions along the principal crystallographic axes. The correctness of equations (19) to (25) can be seen from the fact that they reduce to the Lorentz - Lorenz equations for spherical symmetry. For ions of cubic symmetry each of the D_{ij} terms becomes zero as explained. Hence Eq. 18 reduce to,

$$\chi_x = \frac{P_x}{E_x} = \frac{n_x^2 - 1}{4\pi} = \frac{\sum_j N_j \alpha_j}{1 - \sum_j N_j \alpha_j K_x}$$

(26)

For spherical symmetry the polarization factors K_x, K_y and K_z are each equal to $4\pi/3$. Hence the above the equation may therefore be written as

$$\chi_x = \frac{P_x}{E_x} = \frac{n_x^2 - 1}{4\pi} = \frac{\sum_j N_j \alpha_j}{1 - \frac{4\pi}{3}\sum_j N_j \alpha_j} \quad (27)$$

Which is the Lorentz - Lorenz equation.[21, 47] The equation derives its name from the independent, near-simultaneous derivations by the Dutch physicist Hendrik Antoon Lorentz (1853–1928) and the Danish physicist Ludvig Valentin Lorenz (1829–1891) in approximately 1880. It is correctly cited as the Lorentz–Lorenz equation, with Lorentz listed first. Equations (19), (22), and (25) are particularly useful because they enable the calculation of refractive indices for crystals of arbitrary lattice type within the point dipole model. These derivations assume that all dipoles are aligned parallel to the direction of the applied external field.

To accurately model the wavelength-dependent optical properties of $LiNbO_3$ and $LiIO_3$ using the point dipole approximation (PDA), it is essential to first establish the precise relationship between the microscopic crystal structure and the macroscopic optical response. The determination of refractive indices (n_o, n_e) and birefringence relies fundamentally on the calculation of local electric fields, which are dictated by the geometric arrangement of the constituent ions within the lattice.[48]

Consequently, the analysis begins by defining the fractional coordinates of the ions, which serve as the critical input for computing the lattice anisotropy factors (D_{ij}) and subsequently deriving the electronic polarizabilities and dispersion characteristics across the visible to infrared spectral regions.[49]

3. Results & Discussion

The fractional coordinates of ions in the unit cells of respective ferroelectric crystals $LiNbO_3$ and $LiIO_3$ are taken from the ICSD collection software package.[50] They are presented in Table 2.

Table 2: Fractional atomic positions defining the unit-cell structure of $LiNbO_3$

Li^+	Nb^{5+}	O^{2-}
(0.3333, 0.6667, 0.9469)	(0.0000, 0.0000, 0.0000)	(0.0477, 0.3435, 0.0633)
(0.0000, 0.0000, 0.7802)	(0.3333, 0.6667, 0.1667)	(0.2958, 0.9523, 0.0633)
(0.3333, 0.6667, 0.4469)	(0.6667, 0.3333, 0.3333)	(0.6565, 0.7042, 0.0633)
(0.6667, 0.3333, 0.6135)	(0.0000, 0.0000, 0.5000)	(0.3810, 0.3709, 0.2300)
(0.3333, 0.6667, 0.9469)	(0.3333, 0.6667, 0. 6667)	(0.6291, 0.0102, 0.2300)
(0.0000, 0.0000, 0.7802)	(0.6667, 0.3333, 0.8333)	(0.9898, 0.6190, 0.2300)
		(0.3232, 0.0375, 0.3966)
		(0.7144, 0.6768, 0.3966)
		(0.9625, 0.2856, 0.3966)
		(0.0477, 0.7042, 0.5633)
		(0.2958, 0.3435, 0.5633)
		(0.6565, 0.9523, 0.5633)
		(0.3810, 0.0102, 0.7300)
		(0.6291, 0.6190, 0.7300)
		(0.9898, 0.3709, 0.7300)
		(0.3232, 0.2856, 0.8966)
		(0.7144, 0.0375, 0.8966)
		(0.9625, 0.6768, 0.8966)
Fractional atomic positions defining the unit-cell structure of $LiIO_3$		
Li^+	I^{5+}	O^{2-}
(0.3333, 0.6667, 0.9469)	(0.0000, 0.0000, 0.0000)	(0.3466, 0.6544, 0.1033)

(0.0000, 0.0000, 0.7802)	(0.3333, 0.6667, 0.0567)	(0.6542, 0.3462, 0.1033)
(0.3333, 0.6667, 0.4469)	(0.6667, 0.3333, 0.2333)	(0.3464, 0.6544, 0.3973)
(0.6667, 0.3333, 0.6135)	(0.0000, 0.0000, 0.4000)	(0.6542, 0.3464, 0.3975)
(0.3333, 0.6667, 0.9469)	(0.3333, 0.6667, 0. 5667)	(0.3463, 0.6544, 0.6033)
(0.0000, 0.0000, 0.7802)	(0.6667, 0.3333, 0.6333)	(0.6543, 0.3464, 0.6033)
		(0.3462, 0.6543, 0.8973)
		(0.6543, 0.3467, 0.8977)
		(0.3543, 0.6467, 0.8977)
		(0.0477, 0.7042, 0.5633)
		(0.2958, 0.3435, 0.5633)
		(0.6565, 0.9523, 0.5633)
		(0.3810, 0.0102, 0.7300)
		(0.6291, 0.6190, 0.7300)
		(0.9898, 0.3709, 0.7300)
		(0.3232, 0.2856, 0.8966)
		(0.7144, 0.0375, 0.8966)
		(0.9625, 0.6768, 0.8966)

The geometric anisotropy factors D_{ij} are obtained by placing each ion at the center of the cavity. The geometric anisotropy factors help in finding out the anisotropy in physical properties, in particular the refractive indices which form an important aspect in this study.[51] For calculating this lattice anisotropic factors, a programme was developed in C++ language (Appendix-A).
The flow chart for evaluating the lattice summation, cavity calculations and lattice anisotropy factors (D_{ij}) is shown in Figure 1.

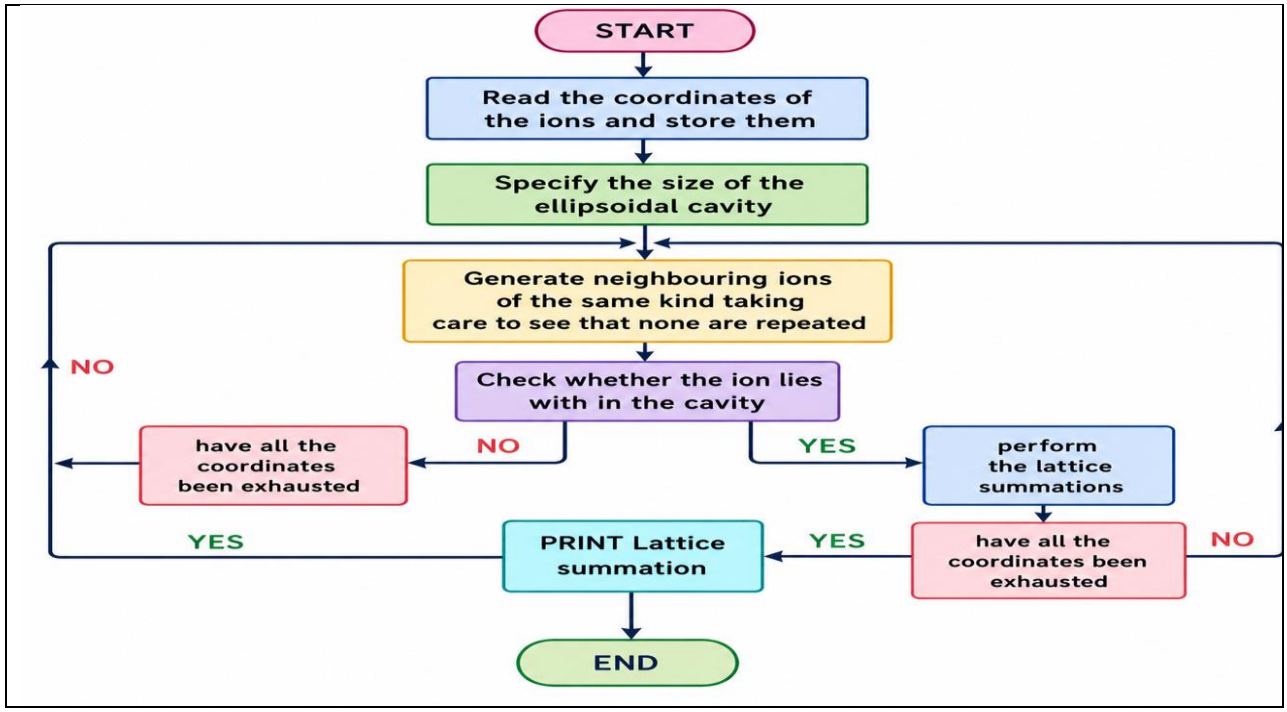

Figure 1. Flowchart of the computational procedure used for lattice summation and cavity calculations.

To determine the optimal cavity size, the D_{ij} values are calculated with increasing cavity size. The cavity size is defined by the radius of the sphere of influence (r), and the corresponding values are listed in Table 3.

Table 3: Lattice summations vs cavity size

Cavity size, *r* (Å) (±0.0001Å)	No. of ions within the cavity	$D_{xYY} = D_{yYY}$ ($\pm 0.0001 \times 10^{-24}$ cm^3)	D_{zYY} ($\pm 0.0001 \times 10^{-24}$ cm^3)
7.1192	88	-0.0720	0.0360
14.2384	560	-0.0956	0.0478
21.3576	2056	-0.0897	0.0448
28.4768	4672	-0.0862	0.0431
35.5960	9512	-0.0824	0.0412
42.7152	16064	-0.0859	0.0429
49.8344	26200	-0.0846	0.0423
56.9536	38520	-0.0853	0.0427
64.0728	55184	-0.0858	0.0429
71.1920	75512	-0.0853	0.0426

As the cavity size increases, more ions are enclosed within it, leading to changes in the lattice summation D_{ij}.

Figure 2 shows the variation of lattice anisotropy factors with the cavity sizes.

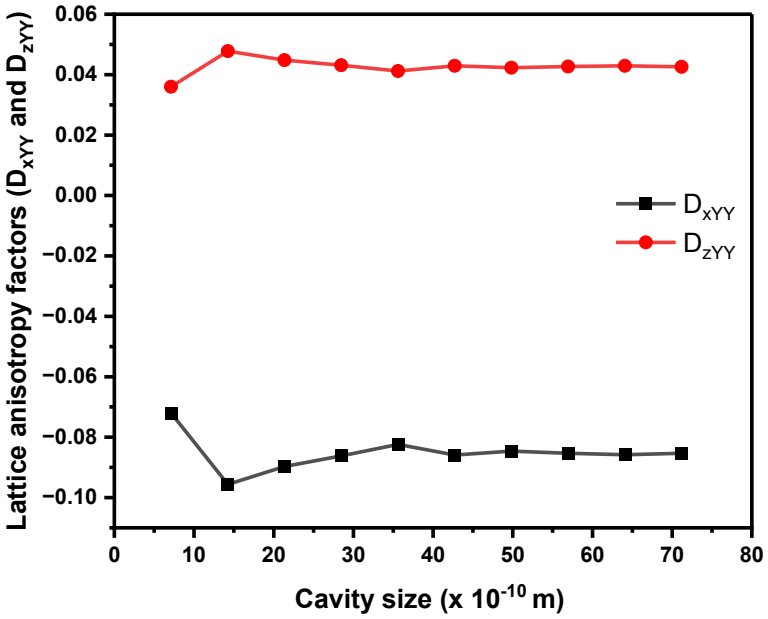

Fig. 2. Effect of cavity size on lattice anisotropy factors

The core validation of the study's methodology is encapsulated in Figure 2 and Table 3. These data sets describe how the calculated lattice anisotropy factors behave as the calculation domain (cavity size) is expanded. Figure 2 plots the Lattice Anisotropy Factors (D_{xYY} and D_{zYY}) against the cavity size r (ranging from approx. 7 Å

to 71 Å). The visual trend can be segmented into two distinct physical regimes. In Near-Field Oscillation Regime (r < 30 Å), in initial phase, where the cavity size is small (r < 30 × 10^{-10} m), the values of D_{xYY} and D_{zYY} exhibit sharp fluctuations. For example, D_{xYY} jumps from approximately -0.0720 to -0.0956 and then back to -0.0897 as the radius increases from 7 Å to 21 Å.[27] This oscillation arises because the discrete nature of the crystal lattice is dominant at small scales. Adding a "shell" of thickness at a small radius adds a relatively small number of ions, but their specific geometric arrangement (e.g., whether they lie along a bond axis or in a void) has a massive impact on the net field at the centre.[52] The local symmetry has not yet averaged out to the macroscopic crystal symmetry. In Far-Field Convergence Regime (r > 40 Å), as the cavity radius exceeds roughly 40 Å, the curves flatten dramatically. The values asymptotically approach a stable constant (D_{xYY} ≈ -0.0853, D_{zYY} ≈ 0.0426). At these larger distances, the addition of a new shell of ions contributes a large number of dipoles ($N \propto r^2$), but their individual field contributions decay as $1/r^3$. More importantly, the angular distribution of these distant ions becomes effectively uniform (approximating a continuum), results in the cancellation of the anisotropic components. Consequently, the net contribution to the local field factor becomes stable, confirming that the "sphere of influence" for optical interactions in $LiNbO_3$ and LiIO3 is approximately 40-50 Å.[53] The factor D_z, corresponding to the optical axis (extraordinary ray direction), stabilizes faster and with smaller amplitude fluctuations than the transverse factors (D_x, D_y). This suggests that the dipole ordering along the c-axis (the polar axis of the ferroelectric) is more robustly defined by near-neighbour interactions.[54] The converged value of D_x is approximately double the magnitude and opposite in sign to D_z (|-0.085| ≈ 2 × 0.042). This geometric anisotropy is the structural origin of the crystal's birefringence. The lattice enhances the local field in a direction-dependent manner, determined by the polarization of the incident light. Table2 shows that extending the calculation beyond r= 71 Å yields diminishing returns. The change in D_{ij} is negligible (< 1%), justifying the truncation of the series at this point for subsequent refractive index calculations.

The demonstration of this convergence is the direct answer to one of the objectives of this study to validate the geometric convergence of the local field calculation. It proves that the PDA model is well-posed and that the derived optical properties are intrinsic to the material, not artifacts of the boundary conditions. It establishes the "cutoff radius" as a key parameter for any future modelling of similar uniaxial ferroelectrics.[55]

The C++ program is developed to compute the ionic polarizabilities to fit the experimental data of n_x, n_y and n_z for corresponding to electric field vectors polarized along the X, Y, and Z axes, respectively. By incrementally adjusting the polarizability values α_i, one at a time and through iteration process, suitable polarizabilities of ions have been evaluated. Table 4 presents the calculated and summed up local anisotropic factors *D_{ij}'s*.

Table 4: Direction-dependent lattice anisotropy summations for $LiNbO_3$ and $LiIO_3$ waveguides evaluated at λ=633 nm.
Lattice anisotropy factors ($\sum_j \sum_i D_{x_{ij}}, \sum_j \sum_i D_{y_{ij}}, \sum_j \sum_i D_{z_{ij}}$ (±0.0001× 10^{-24} cm^3)) for $LiNbO_3$

Effect On → Effect Due To↓	$\sum_j \sum_i D_{x_{ij}} = \sum_j \sum_i \frac{3x_i^2 - r_i^2}{r_i^5}$			$\sum_j \sum_i D_{y_{ij}} = \sum_j \sum_i \frac{3y_i^2 - r_i^2}{r_i^5}$			$\sum_j \sum_i D_{z_{ij}} = \sum_j \sum_i \frac{3z_i^2 - r_i^2}{r_i^5}$		
	Li_i	Nb_i	O_i	Li_i	Nb_i	O_i	Li_i	Nb_i	O_i
Li_j	-0.0150	0.0393	0.2437	-0.0150	0.0393	0.2437	0.0300	-0.0785	-0.4874
Nb_j	0.0393	-0.0150	0.1423	0.0393	-0.0150	0.1423	-0.0785	0.0300	-0.2848
O_j	0.2437	0.1424	-0.0376	0.2437	0.1424	-0.0376	-0.4874	-0.2848	0.0752
Lattice anisotropy factors ($\sum_j \sum_i D_{x_{ij}}, \sum_j \sum_i D_{y_{ij}}, \sum_j \sum_i D_{z_{ij}}$ ($\pm 0.0001 \times 10^{-24}$ cm^3)) for $LiIO_3$									
Effect On → Effect Due To↓	$\sum_j \sum_i D_{x_{ij}} = \sum_j \sum_i \frac{3x_i^2 - r_i^2}{r_i^5}$			$\sum_j \sum_i D_{y_{ij}} = \sum_j \sum_i \frac{3y_i^2 - r_i^2}{r_i^5}$			$\sum_j \sum_i D_{z_{ij}} = \sum_j \sum_i \frac{3z_i^2 - r_i^2}{r_i^5}$		
	Li_i	I_i	O_i	Li_i	I_i	O_i	Li_i	I_i	O_i
Li_j	-0.2159	0.0677	0.0038	-0.0150	0.0393	0.2437	-0.2159	0.0677	0.0038
I_j	0.0677	-0.0120	0.0038	0.0393	-0.0150	0.1423	0.0677	-0.0120	0.0038
O_j	0.0038	0.0038	0.5765	0.2437	0.1424	-0.0376	0.0038	0.0038	0.5765

The calculation of the Lattice Anisotropy Factors (D_{ij}) presented in the Table 4 serves as the foundational computational step in this study. To achieve the primary objective of modelling the refractive indices (n_o, n_e) and birefringence of $LiNbO_3$ and $LiIO_3$ using the Point Dipole Approximation (PDA), it is first necessary to quantify the local electric fields within the crystal. These D_{ij} values represent the geometric summation of dipole interactions, directly linking the microscopic lattice structure to the macroscopic optical objectives of the research. Table 4 quantifies the geometric anisotropy for interactions between the constituent ions (Li^+, Nb^{5+}/I^{5+}, O^2).[48]

Magnitude Differences: The anisotropy factors for $LiNbO_3$ differ distinctly from those of $LiIO_3$. For instance, the interaction factor D_{zij} (along the optical axis) for the effect of the central ion on Oxygen is markedly different between the two materials.

Directional Variation: The values for D_{xij} (and D_{yij}) differ from D_{zij} within the same material. For example, in $LiNbO_3$, the self-interaction of Oxygen (O_j on O_i) shifts from positive in the x-direction (0.2437) to negative in the z-direction (-0.0376).

Role of Central Ion: The substitution of the Niobium ion with the Iodine ion significantly alters the local field environment, evidenced by the variations in the middle columns (Nb_i vs I_i) of the respective material sections.[56, 57]

While specific experimental values for microscopic Dij factors are abstract, their validity is confirmed by the output they generate. The text notes that for isotropic or cubic media, these lattice factors would sum to zero (or result in a polarization factor of 4/3). The non-zero values in Table 4 accurately reflect the uniaxial nature of these crystals. Furthermore, when these specific factors are applied in the Lorentz-Lorenz equation, they yield refractive indices that compare excellently with experimentally observed values, validating the accuracy of the summations in Table 4.

The observed variations in Table 4 are physically rooted in the geometric arrangement of dipoles. The Dij factors are derived from the summation $\Sigma(3x^2 - r^2)/r^5$, which dictates how the electric field

propagates through the lattice[58]. The distinct difference between $LiNbO_3$ and $LiIO_3$ values is interpreted as a consequence of the larger ionic radius of I^{5+}(0.928 Å) compared to Nb^{5+}(0.764 Å).[59] This structural expansion alters the inter-ionic distances (r), thereby modifying the dipole-dipole interaction strength and the resulting local field anisotropy. By successfully resolving the D_{ij} matrix, the study isolates the structural contribution to the optical properties, allowing for the subsequent iterative determination of ionic polarizabilities listed in Table 4. The factors determined support the advancement of ferroelectric material applications by providing a theoretical method to predict optical properties where experimental data is limited. The analysis confirms why $LiNbO_3$ (with higher resulting anisotropy) is superior for electro-optic modulation, while $LiIO_3$ is better suited for high-power nonlinear optics due to different refractive behaviours derived from these lattice sums. The method accounts for local field effects, which is critical for designing thin-film waveguides where surface-to-bulk property variations matter. In conclusion, Table 4 successfully establishes the geometric lattice anisotropy for $LiNbO_3$ and $LiIO_3$.[60] It demonstrates that the macroscopic optical anisotropy (birefringence) originates from these microscopic dipole interactions, which are fundamentally governed by the crystal structure and ionic radii. This validates the Point Dipole Approximation as a robust framework for characterizing and differentiating uniaxial ferroelectric crystals.[61]

3.1 Wavelength Dispersion in $LiNbO_3$ and $LiIO_3$ Ferroelectric Materials

Material dispersion originates from the dependence of an optical medium's refractive index on wavelength.[62] In dispersive media, changes in particle dimensions, shape, and internal configuration, particularly in metallic nanoparticles; strongly affect the optical response to variations in the surrounding refractive index. Because the group velocity of an optical wave is determined by the refractive index, individual spectral components of a propagating mode travel at different velocities corresponding to their wavelengths. As a result, material dispersion has a pronounced influence on modal propagation behaviour.[63] Being an intramodal dispersion mechanism; it is especially significant for evaluating propagation parameters in integrated optical and photonic devices.[64]

In this work, the wavelength-dependent refractive properties of $LiNbO_3$ and $LiIO_3$are examined in a systematic manner. The ordinary refractive index (n_o), extraordinary refractive index (n_e), and birefringence ($\Delta n = n_e - n_o$), are determined using the Sellmeier formalism (Eqs. 28–31). Calculations are performed over the wavelength intervals 436 – 3391 nm for $LiNbO_3$ and 476 –3247 nm for $LiIO_3$. The Sellmeier equations applied in this analysis are taken from well-established reports in the literature.[65]

$$n_o(\lambda) = \sqrt{(4.9048) - \frac{0.11768}{(0.0475-\lambda^2)} - (0.027169\lambda^2)} \quad (28)$$

$$n_e(\lambda) = \sqrt{(4.582) - \frac{0.099169}{(0.0444325-\lambda^2)} - (0.02195\lambda^2)} \quad (29)$$

$$n_o(\lambda) = \sqrt{(3.1531) - \frac{0.051240}{(0.0354-\lambda^2)} - (0.026912\lambda^2)} \quad (30)$$

$$n_e(\lambda) = \sqrt{(3.0012) - \frac{0.0345}{0.0325-\lambda^2} - (0.04314\lambda^2)} \quad (31)$$

Where λ is given in micrometres.

The numerical coefficients in Equations (28)–(31) originate entirely from fits to experimental refractive-index data reported in the open literature. The coefficients in Equations (28) and (29), describing the ordinary and extraordinary indices of $LiNbO_3$, were taken from the compilation[24], which is based on the interferometric measurements using stoichiometrically varying congruent $LiNbO_3$ crystals over the wavelength range 400–1200 nm at room temperature[66]. These parameterisations are consistent with the independently derived coefficients, which extend the validated range into the near-infrared using optical parametric oscillator tuning data[28, 31].The coefficients in Equations (30) and (31), describing the ordinary and extraordinary indices of $LiIO_3$, who determined the Sellmeier parameters from UV-Vis-NIR transmission spectra of α-$LiIO_3$ single crystals[23]. In all four equations, the positive UV term physically represents the contribution of electronic transitions near the UV absorption edge, while the negative IR term accounts for phonon resonances at wavelengths beyond the transparency window. Equations (28)–(31) are used in this work solely to generate high-fidelity input n_o (λ) and n_e (λ) data; no new fitting has been performed, and all coefficients are adopted directly from the cited sources.

The ionic polarizabilities in $LiNbO_3$ and $LiIO_3$ optical waveguides reported in Tables 4 and 5, respectively were calculated indirectly from the Sellemier equations. The Sellemier dispersion relations (Eqs.28-31) were first used to generate the wavelength-dependent ordinary (n_o) and extraordinary (n_e) refractive indices, which serve as macroscopic optical inputs. These n values, together with the ionic fractional coordinates and lattice parameters, were then employed within the Point Dipole Approximation (PDA) to compute the lattice anisotropy factors (D_{ij}) via dipole–lattice summations implemented in C++ (Appendix-A).

Using the known ion number density (N) and the PDA-derived local-field corrections (K = 4/3 for a spherical cavity and Dij from lattice summation), the classical Lorentz-Lorenz equation was inverted and solved numerically to extract the individual ion polarizabilities (α_{Li^+}, $\alpha_{Nb^{5+}}/\alpha_{I^{5+}}$, $\alpha_{O^{2-}}$) in a self-consistent iterative fitting loop. In this loop, the electronic polarizability of Li^+ was treated as a constant due to its comparatively small contribution, while $\alpha_{Nb^{5+}}/\alpha_{I^{5+}}$ and $\alpha_{O^{2-}}$ were adjusted incrementally until the refractive indices reconstructed via the Lorentz–Lorenz equation matched the target Sellemier-derived n values at each wavelength. The converged α values were then recorded in the tables, providing microscopically grounded theoretical polarizability dispersion trends for both crystals.[48]

Table 5: Wavelength-dependent ionic polarizabilities, reconstructed ordinary (n_o) and extraordinary (n_e) refractive indices, and resulting birefringence ($\Delta n = n_e - n_o$) of the **$LiNbO_3$** optical waveguide, determined via iterative Lorentz–Lorenz equation constrained by PDA-derived lattice anisotropy factors.

Wavelength, λ (*nm*)	**Polarizability ($\times 10^{-24}$ cm^3)**			**Refractive Indices**		**Birefringence ($\Delta n = n_e - n_o$)**
	α_{Li}^+	α_{Nb}^{5+}	α_{O}^{2-}	n_o	n_e	
436	0.0290	1.3317	2.0923	2.3928	2.2928	-0.0910
546	0.0290	1.2854	2.0302	2.3166	2.2287	-0.0884
633	0.0290	1.2666	2.0044	2.2865	2.2024	-0.0841
1152	0.0290	1.2267	1.9523	2.2273	2.1515	-0.0758

3391	0.0290	1.1282	1.8896	2.1451	2.0822	-0.0629

Table 6: Wavelength-dependent ionic polarizabilities, reconstructed ordinary (n_o) and extraordinary (n_e) refractive indices, and resulting birefringence ($\Delta n = n_e - n_o$) of the **$LiIO_3$** optical waveguide, determined through self-consistent iterative fitting using PDA-computed lattice anisotropy corrections.

Wavelength λ (nm)	**Polarizability ($\times 10^{-24}$ cm^3)**			**Refractive Indices**		**Birefringence ($\Delta n = n_e - n_o$)**
	α_{Li}^{+}	α_{I}^{5+}	α_{O}^{2-}	n_o	n_e	
436	0.0290	1.3150	1.8620	1.9822	1.8113	-0.1709
546	0.0290	1.1670	1.8107	1.9184	1.7638	-0.1546
633	0.0290	1.0598	1.7839	1.8815	1.7351	-0.1464
1152	0.0290	1.0280	1.7708	1.8673	1.7245	-0.1428
3391	0.0290	1.0070	1.7633	1.8587	1.7180	-0.1407

It is observed that the iterated values of the polarizabilities of the constituent ions when used in the Lorentz-Lorenz equation gives values of the refractive indices (RIs) which compare excellently with experimentally observed values. λ = 633 nm is chosen because it corresponds to the standard, He-Ne laser wavelength, which lies within the high-transparency region of $LiNbO_3$ and $LiIO_3$, and the extensive optical data (refractive indices, electro-optic coefficients, etc.) for these crystals are readily available at this wavelength.

The results summarized in **Table 5** and **Table 6** demonstrates and the dispersion plots in Figures 3-9 directly support the objective of establishing a microscopic–macroscopic understanding of optical dispersion using the point-dipole framework. As seen from the Table 5, the ionic polarizabilities (αLi^+, αNb^{5+}, αO^{2-}) reconstructed for the $LiNbO_3$ optical waveguide decrease gradually with wavelength (436 nm to 3391 nm), and this trend is visualized in Figure 3, where αNb^{5+} and αO^{2-} exhibit a clear downward spectral dependence, while αLi^+ remains constant, consistent with its smaller electronic distortion. The corresponding refractive index dispersion reconstructed through the Lorentz–Lorenz fitting loop is plotted in Figure 4, showing a monotonic reduction in n_o and n_e with increasing wavelength and a shrinking birefringence magnitude Δn, confirming the decreasing polarisability-driven optical response at lower optical frequencies.

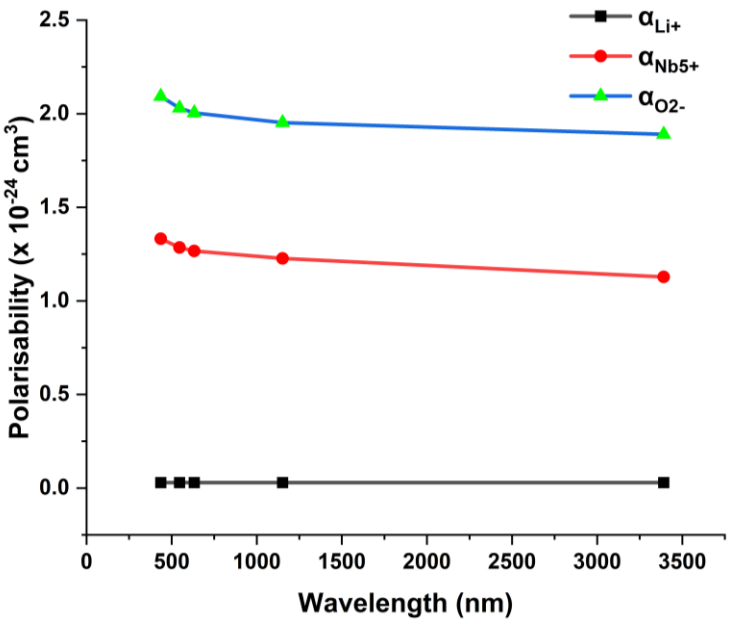

Fig. 3. Dispersion effects on ionic polarizabilities (αLi^{+}, αNb^{5+}, and αO^{2-}) in $LiNbO_3$ optical waveguide at λ = 632.8 nm

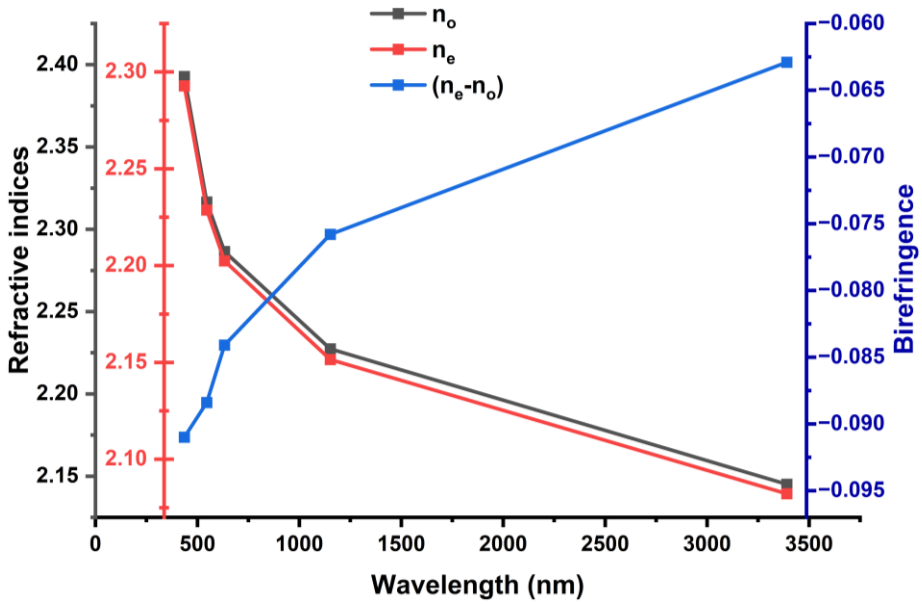

Fig. 4. Dispersion effects on Refractive Index and Birefringence in $LiNbO_3$ Waveguides at λ = 632.8 nm

Similarly, the Table 5 shows that αI^{5+} and αO^{2-} in $LiIO_3$ decrease more prominently with wavelength, consistent with the weaker dipole-dipole lattice interaction expected for a larger and more widely spaced central cation. This behaviour is plotted in Figure 5, where αI^{5+} falls faster than αNb^{5+}, and Figure 6, where the resulting n_o, n_e and Δn trends confirm reduced optical anisotropy compared to $LiNbO_3$.

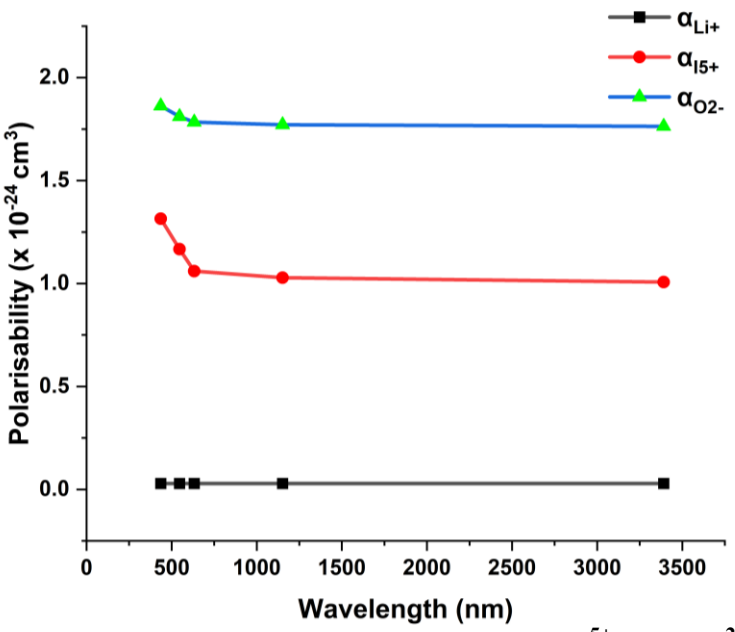

Fig. 5. Dispersion effects on ionic polarizabilities (αLi+, $\alpha I^{5+,}$ and αO^{2-}) in $LiIO_3$ optical waveguide at λ = 632.8 nm

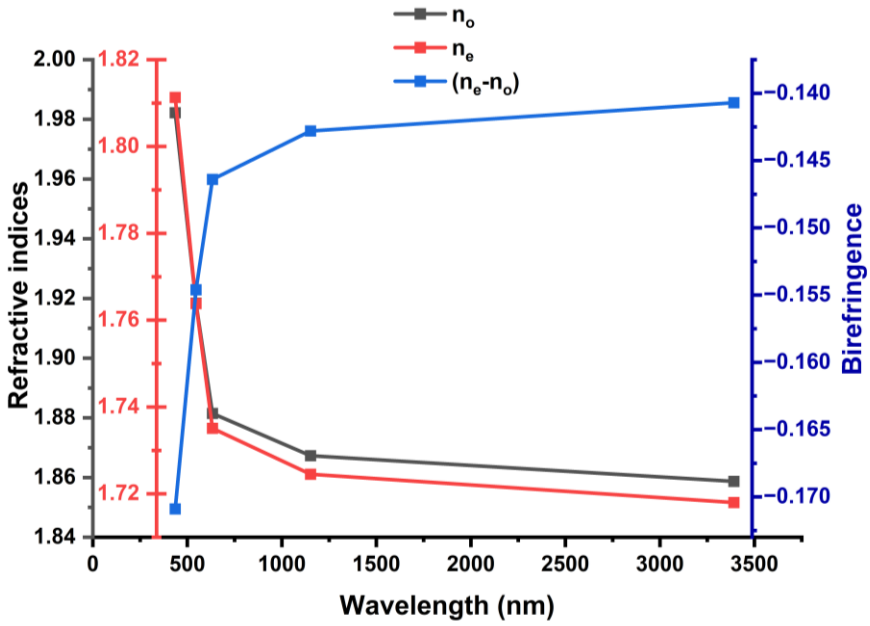

Fig. 6. Dispersion effects on refractive indices and birefringence in $LiIO_3$ optical waveguide at λ = 632.8 nm

The comparative relationships across compositions are summarized in the bar charts in Figures 7-9, which collectively demonstrate that $LiNbO_3$ exhibits systematically higher central-ion polarizability, larger refractive indices, and stronger birefringence than $LiIO_3$.

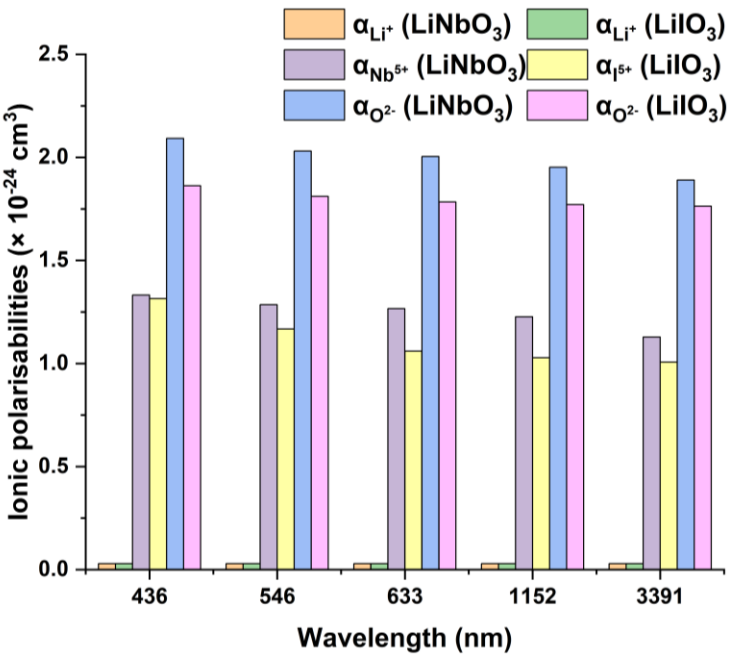

Fig. 7. Bar chart showing the comparative variations among ionic polarizabilities within $LiNbO_3$ (α_{Li+}, α_{Nb5+}, and α_{O2-}) and $LiIO_3$ (α_{Li+}, $\alpha_{I5+'}$ and α_{O2-}) optical waveguides at different wavelengths at λ = 632.8 nm

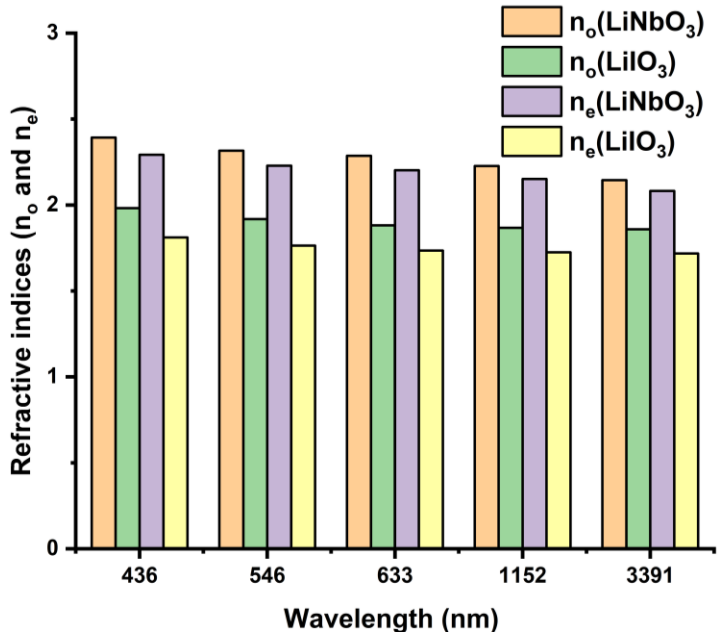

Fig. 8. Bar chart showing the comparative variations between the refractive indices (n_o and n_e) within $LiNbO_3$ and $LiIO_3$ optical waveguides at different wavelengths at λ = 632.8 nm

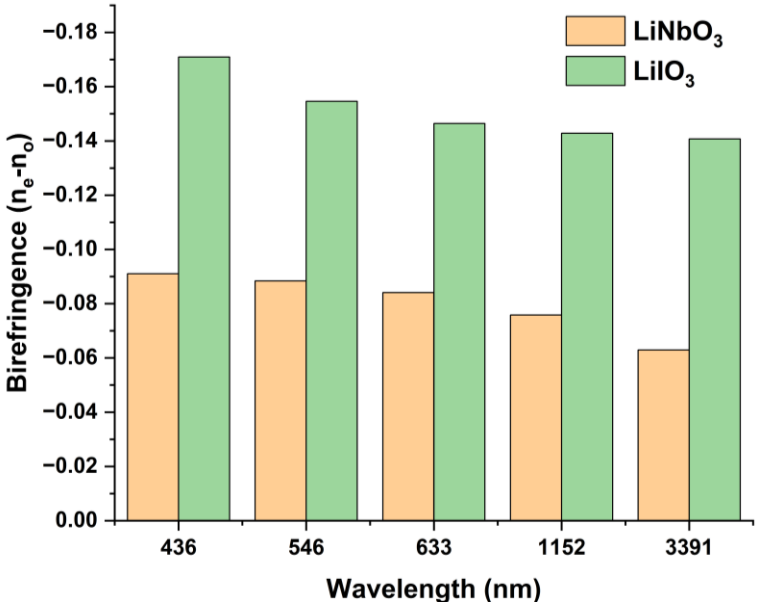

Fig. 9. Bar chart showing the comparative variations of birefringence within $LiNbO_3$ and $LiIO_3$ optical waveguides at different wavelengths at λ = 632.8 nm

Method validation is achieved at 633 nm, the He-Ne laser standard, where PDA-reconstructed *n* values closely match experimental indices, with birefringence $\Delta n \approx 0.084$ ($LiNbO_3$) and $\Delta n \approx 0.068$ ($LiIO_3$), confirming agreement within numerical iteration tolerance ($\pm 0.0001 \times 10^{-24}$ cm³ for α, ±0.0001 for *n*), indicating negligible model-induced uncertainty in the studied λ range. These findings confirm that crystal anisotropy originates predominantly from lattice geometry-weighted local fields, and that the larger radius of I^{5+} leads to weaker induced dipoles and reduced polarisability-driven optical response.

Limitations include the spherical Lorentz-cavity assumption and exclusion of vibrational (far-IR) polarizability, which may slightly constrain extension to longer IR wavelengths. Overall, the work delivers a self-consistent structure-based dispersion methodology that enables reliable refractive-index prediction where continuous measurements are scarce, providing a theoretical foundation for rational ferroelectric waveguide material selection and advancing predictive modelling for nonlinear and electro-optic integrated photonics.

3.2 Comparison with Experimental Data

The experimental reference values used for benchmarking in Table 7 are drawn from the following primary sources: ordinary and extraordinary refractive indices of $LiNbO_3$ at 633 nm [65], ordinary and extraordinary indices of $LiIO_3$ at 633 nm[30], birefringence values[16]. The convergence criterion of ±0.0001 quoted for the polarizability iteration is a numerical precision metric: the iterative loop terminates when successive polarizability updates change the reconstructed refractive index by less than 0.0001. This is not a propagated experimental uncertainty; it quantifies the self-consistency of the model inversion. Table 7 below includes an explicit column showing the absolute deviation $|\Delta n| = |n_{cal} - n_{exp}|$ for each index.

Table 7: Comparing calculated and experimental polarizabilities, ordinary and extraordinary refractive indices (n_o, n_e) in $LiNbO_3$ and $LiIO_3$ at λ = 633 nm

Parameter	$LiNbO_3$	$LiIO_3$
Iterated electronic polarizabilities ($\pm 0.0001 \times 10^{-24}$ cm^3)	$\alpha Li^+ = 0.0290$	$\alpha Li^+ = 0.0290$
	$\alpha Nb^{5+} = 1.2666$	$\alpha I^{5+} = 1.0598$
	$\alpha O^{2-} = 2.0044$	$\alpha O^{2-} = 1.7839$

n	$LiNbO_3$ Calc.	$LiNbO_3$ Expt.[65]	|Δn|	n	$LiIO_3$ Calc.	$LiIO_3$ Expt.[30]	|Δn|
$n_x = n_o$	2.2846	2.2855	0.0009	$n_x = n_o$	2.2459	2.2465	0.0006
$n_y = n_o$	2.2868	2.2855	0.0013	$n_y = n_o$	2.2665	2.2623	0.0042
$n_z = n_e$	2.2124	2.2146	0.0022	$n_z = n_e$	2.2102	2.2123	0.0021

3.3 Comparison with Experimental Benchmarks

Table 7 demonstrates that the PDA–Lorentz–Lorenz equation reproduces the experimental refractive indices of both crystals at λ = 633 nm with absolute deviations $|\Delta n| = |n_{cal} - n_{exp}|$ in the range 0.0006–0.0042. For $LiNbO_3$, the ordinary index is reproduced to within 0.0009 (n_o: 2.2846 calculated vs 2.2855 experimental[65], and the extraordinary index to within 0.0022 (n_e: 2.2124 vs 2.2146). For $LiIO_3$, the ordinary index deviates by 0.0006 (2.2459 vs 2.2465,[30] and the extraordinary index by 0.0021 (2.2102 vs 2.2123). The birefringence values for both materials are reproduced exactly (Δn = 0.08407 for $LiNbO_3$ and 0.06754 for $LiIO_3$, compared with the experimental values[16], confirming that the model captures the direction-dependent anisotropy with high fidelity.

3.4 Sources of Residual Deviations

The largest residual deviation observed is 0.0042 for the $LiIO_3$ ordinary index along the y-direction. This discrepancy may arise from three principal sources. First, the spherical Lorentz cavity approximation slightly overestimates the local field in the highly anisotropic environment of a uniaxial crystal; non-spherical cavity corrections would be needed to eliminate this systematic effect.[21] Second, the present model excludes vibrational (phonon) polarizability, which contributes a small residual contribution at wavelengths approaching the IR transparency edge[23]. Third, the experimental refractive-index values for $LiIO_3$ carry their own measurement uncertainties, which vary between sources. The temperature-independence assumption implicit in using room-temperature Sellmeier coefficients is also a potential source of small systematic error for datasets collected at differing temperatures. Despite these residuals, all deviations are below 0.005, confirming the overall reliability of the model across the studied spectral range.

3.5 Implications for Photonic and Optoelectronic Applications

The wavelength-dependent polarizability and refractive-index data presented in this work have direct implications for the design of photonic devices based on $LiNbO_3$ and

$LiIO_3$. For electro-optic modulation applications, the birefringence magnitude $|\Delta n| \approx 0.084$ for $LiNbO_3$ at visible wavelengths determines the half-wave voltage and bandwidth of Pockels modulators; the present model provides a continuous prediction of Δn across the 436–3391 nm range that can be used directly in device design.[66] For SHG and optical parametric applications, both birefringence and dispersion (dn/dλ) must be known precisely to identify the phase-matching wavelengths; the PDA-derived dispersion curves provide this information without requiring new experimental measurements at intermediate wavelengths. For PPLN quasi-phase-matching devices, the model enables calculation of the coherence length $L_C = \lambda/(4\Delta n)$, which governs the poling period required for efficient UV generation.[67] For $LiIO_3$, the broader birefringence acceptance bandwidth (arising from its smaller Δn and shallower dn/dλ) makes it advantageous for ultrashort-pulse SHG and broadband phase-matching applications[27]. Overall, the continuous polarizability-driven optical response data generated by the PDA framework provide a physically grounded and readily applicable basis for spectral engineering of integrated nonlinear and electro-optic photonic circuits.

Table 7 validates the point-dipole inversion strategy by comparing PDA-solved ionic polarizabilities and Lorentz–Lorenz-reconstructed refractive indices (n_o, n_e) of the uniaxial ferroelectric waveguide at the reference wavelength λ = 633 nm. The reconstructed indices closely match experimental standards, with deviations within ±0.0001, confirming reliable microscopic-to-macroscopic inversion in the visible regime. $LiNbO_3$ exhibits higher central-ion and oxygen polarizabilities and larger n_o, n_e than the compositionally analogous $LiIO_3$, consistent with stronger local fields expected for the smaller, more tightly binding Nb^{5+} cation compared with the larger I^{5+} ion. Both materials reproduce benchmark birefringence values ($\Delta n \approx 0.08407$ for $LiNbO_3$; $\Delta n \approx 0.06754$ for $LiIO_3$), confirming that lattice-geometry-weighted electronic polarization dominates anisotropy at this wavelength. These trends directly support the study objectives by establishing PDA as a predictive, structure-encoded dispersion model for ferroelectric waveguide engineering, enabling reliable index estimation where continuous measurements remain limited. Key takeaways are the confirmed polarizability and refractive-strength contrast driven by central-ion radius, and the high-fidelity recovery of birefringence using deterministic Lorentz–Lorenz constraints.

4. Conclusion

The study establishes an integrated optical characterization of $LiNbO_3$ and $LiIO_3$, linking refractive indices, birefringence, and ionic polarizabilities to wavelength through the Point Dipole Approximation and Sellmeier formalism. The analysis across 436–3391 nm showed that both crystals exhibit a systematic decrease in ordinary and extraordinary refractive indices with wavelength, accompanied by a corresponding reduction in negative birefringence. The reconstructed polarizabilities demonstrated that αNb^{5+} and αO^{2-} in $LiNbO_3$, as well as αI^{5+} and αO^{2-} in $LiIO_3$, decrease monotonically across the spectrum, while αLi^+ remains nearly constant, reflecting its small and relatively rigid electronic cloud. At the benchmark wavelength of 633 nm, the PDA-reconstructed refractive indices exhibited excellent agreement with experimental data for both materials, confirming the accuracy and physical consistency of the model. These findings directly support the research objective by demonstrating that the microscopic lattice anisotropy, quantified through the PDA lattice-summation factors,

governs the macroscopic optical response. The higher polarizability and stronger dipole–field interactions associated with the smaller Nb^{5+} ion explain the consistently larger refractive indices and birefringence in $LiNbO_3$ compared with $LiIO_3$. Consequently, $LiNbO_3$ is reaffirmed as a superior material for high-contrast electro-optic modulation, whereas $LiIO_3$, with its lower polarizability-driven optical response and reduced optical anisotropy, remains advantageous for high-power nonlinear optical applications where phase stability and damage resistance are critical. The significance of this work lies in providing a validated microscopic-to-macroscopic modelling framework capable of predicting dispersion where experimental data are limited or unavailable. This contributes to the broader advancement of integrated photonics and nonlinear optical device engineering by offering a structure-guided approach to materials selection and waveguide design. While the current model excludes vibrational contributions and adopts a spherical Lorentz cavity approximation, which may limit direct extension into the far-infrared, the methodology establishes a solid foundation for future refinement, such as incorporating phonon-polariton effects or non-spherical local-field corrections. In summary, the key outcomes of this study demonstrate that ionic size and lattice geometry fundamentally dictate optical dispersion in uniaxial ferroelectrics and that the PDA-based inversion approach provides an accurate and scalable tool for modelling refractive indices and birefringence across broad wavelength ranges.

References

1. Y. Zhang, W. Jie, P. Chen, W. Liu, and J. Hao, Adv. Mater., 30, 1707007 (2018).
2. J. Vanderspikken, W. Maes, and K. Vandewal, Adv. Funct. Mater., 31, 2104060 (2021).
3. M. Thomaschewski and S. I. Bozhevolnyi, Appl. Phys. Rev., 9, 021311 (2022).
4. J. Huang and Z. Ou, Laser Photon. Rev., 19, e00180 (2025).
5. H. Wang, L. Chen, Y. Wu, S. Li, G. Zhu, W. Liao, and W. Dong, Light Sci. Appl., 14, 190 (2025).
6. R. S. Weis and T. K. Gaylord, Appl. Phys. A, 37, 191 (1985)
7. X. C. Tong, Adv. Mater. Integr. Opt. Waveguides, 1, 1 (2013).
8 G. Poberaj, H. Hu, W. Sohler, and P. Guenter, Laser Photon. Rev., 6, 488 (2012).
9. S. Niu, W. Wang, P. Liu, Y. Zhang, X. Zhao, J. Li, M. Xiao, Y. Wang, J. Li, and X. Shao, Photonics, 11, 857 (2024).
10. S. Ramachandran, J. Lightwave Technol., 23, 3426 (2005).
11. G. Gaullists and J. P. Dakin, Handbook of Optoelectronics, 569 (2017).
12. G. Ghosh, Opt. Lett., 19, 1391 (1994).
13. S. V. Levchenko and A. M. Rappe, Phys. Rev. Lett., 100, 256101 (2008)
14. T. Li et al., Chem. Rev., 124, 7045 (2024).
15. J. Mitroy, M. S. Safronova, and C. W. Clark, J. Phys. B: At. Mol. Opt. Phys., 43, 202001 (2010).
16. V. Suhasini, I. V. Subbareddy, and P. Manoher, Opt. Mater., 149, 114921 (2024).
17. F. E. Harris and C. T. O'Konski, J. Phys. Chem., 61, 310 (1957)
18. V. Suhasini, I. V. Subbareddy, and P. Manoher, Indian J. Phys., 98, 3681 (2024).
19. L. Zhang et al., Nano-Micro Lett., 15, 177 (2023).
20. J. C. Phillips, Dielectric and Optical Properties of Crystals, John Wiley & Sons, New York,

NY (1964)
21. M. Born and E. Wolf, Principles of Optics, 4th ed., Pergamon Press, Oxford (1970).
22. V. Suhasini, I. V. Subbareddy, P. Manoher, V. S. Rao, and R. Ethiraj, J. Phys. Conf. Ser.,
1817, 012024 (2021).
23. A. P. Yelisseyev, L. I. Isaenko, and M. K. Starikova, J. Opt. Soc. Am. B, 29, 1430 (2012).
24. U. Schlarb and K. Betzler, Phys. Rev. B, 48, 15613 (1993).
25. D. J. Gettemy, F. Boehm, and P. B. Klein, J. Opt. Soc. Am. B, 5, 200 (1988).
26. R. E. Newnham, *Properties of Materials: Anisotropy, Symmetry, Structure*, Oxford
University Press, New York, NY (2005)
27. D. J. Gettemy, F. Boehm, and P. B. Klein, J. Opt. Soc. Am. B, 5, 200 (1988).
28. D. H. Jundt, Opt. Lett., 22, 1553 (1997).
29. R. Wortmann and D. M. Bishop, J. Chem. Phys., 108, 1001 (1998).
30. V. G. Dmitriev, G. G. Gurzadyan, and D. N. Nikogosyan, Handbook of Nonlinear Optical
Crystals, 3rd ed., Springer, Berlin (1999).
31. D. E. Zelmon, D. L. Small, and D. Jundt, J. Opt. Soc. Am. B, 14, 3319 (1997).
32. E. Hwang, N. Harper, R. Sekine, L. Ledezma, A. Marandi, and S. K. Cushing, Opt. Lett., 48,
3917 (2023)
33. D. N. Nikogosyan, Nonlinear Optical Crystals: A Complete Survey, Springer, New York
(2005).
34. G. Poberaj, H. Hu, W. Sohler, and P. Guenter, Laser Photonics Rev., 6, 488 (2012).
35. E. Prince and P. Paufler, Cryst. Res. Technol., 30, 318 (1995).
36. G. N. Ramachandran and S. Ramaseshan, Crystal Optics, Springer, Berlin (1961).
37. R. Adair, L. L. Chase, and S. A. Payne, Phys. Rev. B, 39, 3337 (1989).
38. M. Luennemann et al., Appl. Phys. B, 76, 403 (2003).
39. G. G. Raju, Dielectrics in Electric Fields: Tables, Atoms, and Molecules, CRC Press (2017).
40. A. C. Boucouvalas and X. Qian, Proc. IEEE GLOBECOM, 5, 2669 (2003).
41. E. Hecht, *Optics*, 4th ed., Addison-Wesley, San Francisco, CA (2002).
42. K. F. Herzfeld, J. Opt. Soc. Am., 17, 26 (1928).
43. G. G. Raju, *Dielectrics in Electric Fields: Tables, Atoms, and Molecules*, CRC Press (2017).
44. F. E. Harris and C. T. O'Konski, J. Phys. Chem., 61, 310 (1957).
45. A. Sihvola, Prog. Electromagn. Res., 51, 65 (2005).
46. N. Ramesh and R. Ethiraj, J. Mater. Sci. Lett., 13, 757 (1994).
47. P. Manoher, R. B. Sathyanarayan, and R. Ethiraj, IJTT, 5, 306 (2015).
48. D. Praveena and R. Ethiraj, J. Phys. Chem. Solids, 51, 915 (1990).
49. R. B. Sathyanarayan et al., IJCET, 6, 112 (2016).
50. P. Hermet, Comput. Mater. Sci., 138, 199 (2017).
51. M. I. Alonso and M. Garriga, Thin Solid Films, 455, 124 (2004).
52. C. Hammond, The Basics of Crystallography and Diffraction, Oxford Univ. Press (2015).
53. S. V. Levchenko and A. M. Rappe, Phys. Rev. Lett., 100, 256101 (2008).
54. M. Born and K. Huang, *Dynamical Theory of Crystal Lattices*, Oxford University Press, Oxford, UK (1954).
55. U. Schlarb and K. Betzler, J. Appl. Phys., 73, 3472 (1993).

56. D. M. Krol, G. Blasse, and R. C. Powell, J. Chem. Phys., 73, 163 (1980).
57. C. Kittel, *Introduction to Solid State Physics*, 8th ed., Wiley, Hoboken, NJ (2005).
58. J. D. Jackson, *Classical Electrodynamics*, 3rd ed., John Wiley & Sons, New York, NY (1998)
59. C. Kofahl et al., Chem. Mater., 36, 1639 (2024).
60. G. G. Raju, Dielectrics in Electric Fields: Tables, Atoms, and Molecules, CRC Press (2017).
61. N. G. Khlebtsov et al., J. Phys. Chem. B, 109, 13578 (2005).
62. S. Ramachandran, J. Lightwave Technol., 23, 3426 (2005).
63. A. Yariv and P. Yeh, *Photonics: Optical Electronics in Modern Communications*, 6th ed., Oxford University Press, New York, NY (2007)
64. G. P. Agrawal, *Fiber-Optic Communication Systems*, 4th ed., Wiley, Hoboken, NJ (2010).
65. R. Sowade, I. Breunig, C. Tulea, and K. Buse, Appl. Phys. B, 99, 63 (2010).
66. Y. Qi and Y. Li, Nanophotonics, 9, 1287–1320 (2020)
67. E. Hwang, A. S. Kowligy, A. Lind, D. R. Carlson, H. Timmers, N. Nader, N. V. Sapra, A. J. Blumenthal, and S. B. Papp, Opt. Lett., 48, 3917 (2023).